

High-Strain Peano-HASEL Actuators

Xingrui Wang, Shane K. Mitchell, Ellen H. Rumley, Philipp Rothmund, and Christoph Keplinger*

Soft robots are intrinsically safe for use near humans and adaptable when operated in unstructured environments, thereby offering capabilities beyond traditional robots based on rigid components. Soft actuators are key components of soft robots; recently developed hydraulically amplified self-healing electrostatic (HASEL) actuators provide a versatile framework to create high-speed actuators with excellent all-around performance. Peano-HASEL actuators linearly contract upon application of voltage, closely mimicking the behavior of muscle. Peano-HASEL actuators, however, produce a maximum strain of $\approx 15\%$, while skeletal muscles achieve $\approx 20\%$ on average. Here, a new type of HASEL is introduced, termed high-strain Peano-HASEL (HS-Peano-HASEL) actuator, that achieves linear contraction up to $\approx 24\%$. A wide range of performance metrics are investigated, and the maximum strain of multiunit HS-Peano-HASEL actuators is optimized by varying materials and geometry. Furthermore, an artificial circular muscle (ACM) based on the HS-Peano-HASEL acts as a tubular pump, resembling the primordial heart of an ascidian. Additionally, a strain-amplifying pulley system is introduced to increase the maximum strain of an HS-Peano-HASEL to 42%. The muscle-like maximum actuation strain and excellent demonstrated all-around performance of HS-Peano-HASEL actuators make them promising candidates for use in artificial organs, life-like robotic faces, and a variety of other robotic systems.

1. Introduction

Rigid robots have dominated the field of robotics for decades because of their accuracy, speed, and strength. These features make them well suited for industrial mass production, yet they experience challenges performing versatile and delicate

tasks due to their rigidity and overall lack of adaptability.^[1] In contrast, soft robots use flexible components to avoid these drawbacks and to expand the capabilities of traditional robots.^[2–5] In particular, soft actuators enable soft robots to perform complex motion and can be used in devices that directly interact with the human body.^[6]

Dielectric elastomer actuators (DEAs)^[7–11] and pneumatic artificial muscles (PAMs)^[12–15] are highly developed soft actuators; DEAs exhibit high strain^[16] and speed^[7,17] and the capability to self-sense,^[18] but they suffer from permanent failure due to dielectric breakdown, which becomes more likely when the actuators are scaled up;^[19] PAMs can achieve high actuation stress^[20] and offer many different types of motion,^[21–24] but they are challenging to precisely control. Further, PAMs usually have to be tethered to a high-pressure source^[25] to provide rapid motion, limiting their potential use in highly agile autonomous robots.^[26] Recently developed hydraulically amplified self-healing electrostatic (HASEL) actuators combine the speed and self-sensing

ability of DEAs and the versatility of PAMs while avoiding important drawbacks by utilizing an electrohydraulic principle to locally displace a hydraulic fluid and by being able to self-heal from electric damage.^[27] Additionally, their combination of speed, efficiency, and versatility makes them promising candidates for use in untethered systems.^[28]


Peano-HASEL actuators, one type of HASEL actuator, exhibit fast and precise linear contraction that closely resembles the movement of natural muscle, and they are predicted to exceed the energy density of muscle;^[29,30] therefore, they are well suited as actuators in bioinspired and biomimetic systems. However, the maximum theoretical strain of Peano-HASEL actuators is 24%, and only $\approx 15\%$ strain has been demonstrated experimentally,^[29] while natural muscle typically operates at 20% strain and achieves maximum strain of up to 40%.^[31]

Here, we introduce a new design of HASEL actuators, termed high-strain Peano-HASELs (HS-Peano-HASELs), that can linearly contract up to 36% theoretically. Experimentally, the actuator achieved a maximum linear contraction of $\approx 24\%$ under a load of 0.2 N. As a trade-off, the blocking force of the actuator reduced to 18 N compared to a Peano-HASEL actuator (65 N) with similar specific energy. The

X. Wang
School of Physics Science and Engineering
Tongji University
1239 Siping Road, Shanghai 200092, China

X. Wang, S. K. Mitchell, E. H. Rumley, Dr. P. Rothmund, Prof. C. Keplinger
Department of Mechanical Engineering
University of Colorado, Boulder
1111 Engineering Drive, Boulder, CO 80309, USA
E-mail: Christoph.Keplinger@colorado.edu

Prof. C. Keplinger
Materials Science and Engineering Program
University of Colorado, Boulder
1111 Engineering Drive, Boulder, CO 80309, USA

 The ORCID identification number(s) for the author(s) of this article can be found under <https://doi.org/10.1002/adfm.201908821>.

DOI: 10.1002/adfm.201908821

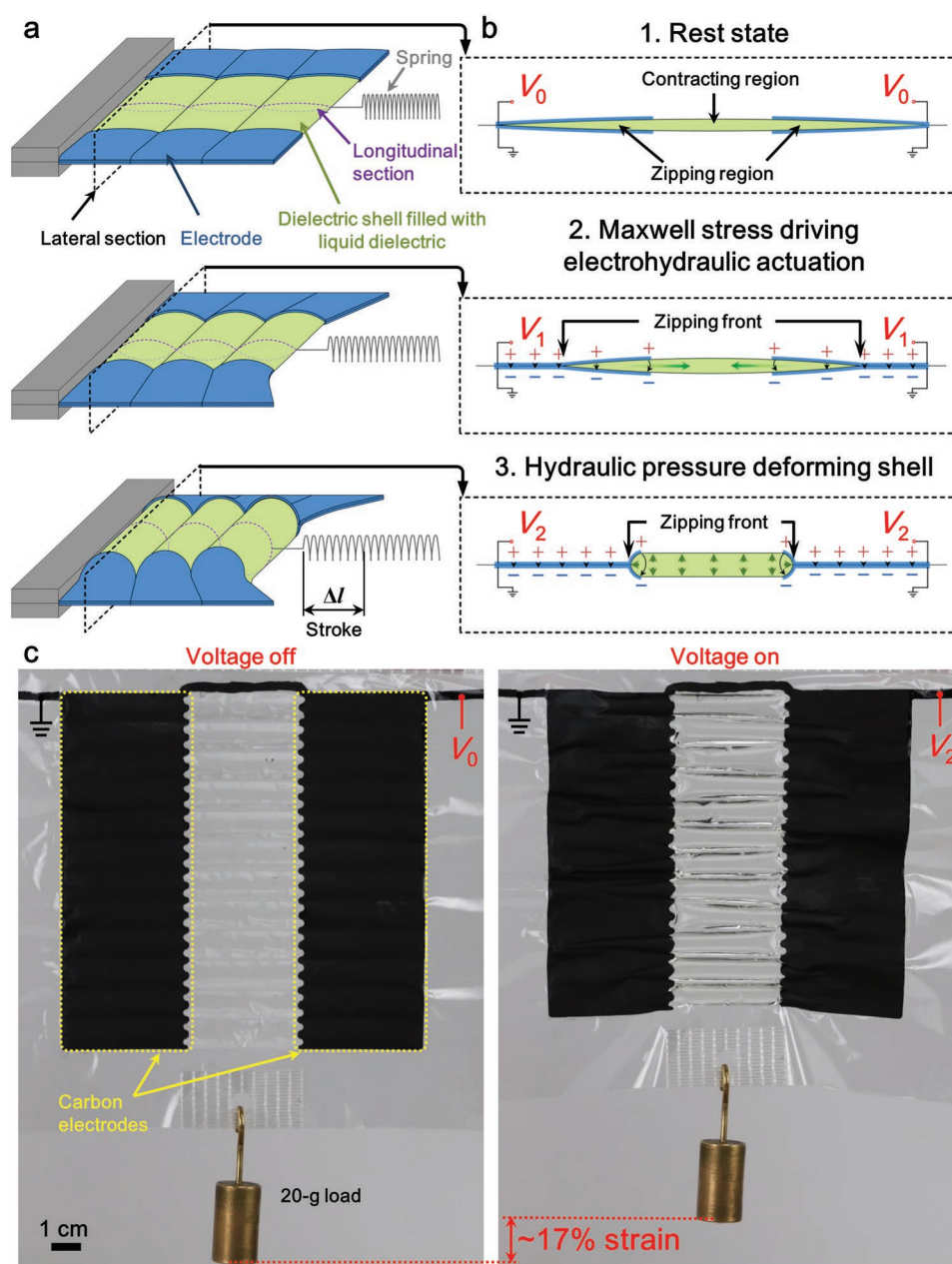


Figure 1. Design of high-strain Peano-HASEL (HS-Peano-HASEL) actuators and principle of operation. a) Schematic aerial view showing a three-unit HS-Peano-HASEL actuator connected to a spring acting as a load. In each unit, electrodes are placed on the ends of the rectangular shell. b) When applying an increasing voltage ($V_0 < V_1 < V_2$) to the electrodes, electrostatic pressure (Maxwell stress) drives the liquid dielectric from the zipping region (the region covered by electrodes) to the contracting region. This process increases the hydraulic pressure within the shell and leads to the contracting region deforming into a cylindrical shape. This deformation results in a linear contraction of the actuator. c) Operated at $V_2 = 10$ kV, a 12 unit HS-Peano-HASEL actuator achieved $\approx 17\%$ strain while lifting a 20 g load.

HS-Peano-HASEL actuator demonstrated excellent overall performance, combining large strain and wide bandwidth with a peak strain rate of $2176\% \text{ s}^{-1}$ and a specific power of 118 W kg^{-1} . Through exploring HS-Peano-HASEL actuators based on different materials and electrode geometries, we show that multiple actuators can be effectively connected in series to achieve large actuation strokes; we utilized this large stroke to create a bioinspired artificial circular muscle (ACM) that operated as a soft pump.

2. Results

2.1. Design of HS-Peano-HASEL Actuators

HS-Peano-HASEL actuators consist of rectangular polymer shells that are filled with a liquid dielectric, and are, except for a region in the center of the shells, coated on both sides with electrodes (Figure 1a). The design divides an actuator into two parts, the zipping region and the contracting region (Figure 1b). When

a voltage is applied to the electrodes, a Maxwell stress causes the electrodes to zip together from the ends displacing the liquid dielectric into the contracting region. The hydraulic pressure in the shell increases. The cross section of the contracting region becomes more circular and the actuator contracts (Figure 1a,b).

This design is different from previously reported Peano-HASEL actuators (Figure S1, Supporting Information).^[30] For Peano-HASEL actuators, the electrode covers the top half of the shell across the entire width. The zipping region and the contraction region are therefore aligned in the direction of contraction. Thus, the zipping region contributes to the initial length of the actuator but does not contract during actuation, and consequently the maximum theoretical actuation strain of Peano-HASEL actuators is limited to 24%.^[29] In HS-Peano-HASEL actuators, the zipping regions and the contracting region are aligned orthogonally to the direction of contraction, and therefore do not contribute to the initial length (Figure 1a). For that reason, HS-Peano-HASEL actuators can achieve a maximum theoretical actuation strain of 36% (see the Supporting Information for calculation).

2.2. Performance of HS-Peano-HASEL Actuators

2.2.1. Quasistatic Characteristics

We measured the load–strain characteristics of a single unit HS-Peano-HASEL actuator (Figure 2a). For comparison, we also measured the load–strain curve of a single-unit Peano-HASEL actuator with the same mass, materials, shell length, and maximum capacitance when electrodes are fully zipped (Figure 2a). With these design choices, the specific energy of both actuators should be the same theoretically. At small loads (<6 N), the HS-Peano-HASEL actuator showed larger strains than the Peano-HASEL actuator (Figure 2b). The maximum strain of the HS-Peano-HASEL actuator was 23.58% whereas the maximum strain of the Peano-HASEL actuator was 8.96% under a load of 0.2 N. At large loads (>6 N), the actuation strain of the Peano-HASEL actuator exceeded the actuation strain of the HS-Peano-HASEL actuator (Figure 2c). The blocking force of the Peano-HASEL actuator (65 N) was larger than the blocking force of the HS-Peano-HASEL actuator (18 N). This decrease of the blocking force can be explained with energetic considerations. Because both actuators were designed to have the same maximum capacitance (when the electrodes are fully zipped together), shell length, and mass, they ideally have not only the same specific energy but also the same area under the load–strain curve. Thus, increasing the strain of the actuator leads to a decrease of the maximum load. The experimentally measured specific energy of the Peano-HASEL actuator was 4.93 J kg^{−1} and of the HS-Peano-HASEL actuator was 4.03 J kg^{−1}. We hypothesize that the difference in specific energy stems from the mechanical constraints due to the buckling in the transition zones between the zipping and contracting regions in the HS-Peano-HASEL actuator.

2.2.2. Analytical Model

To better understand the quasistatic behavior of HS-Peano-HASEL actuators, we derived an electromechanical model for

the actuator. In the model, we neglected the elasticity of the shell, the electric field inside of the contracting region where the electrodes are not fully zipped, and the effects of constraints at the sides of the shell as well as the constraints at the transition zone between the zipping and contracting regions. By minimization of the free energy of the actuator, we derived analytic equations for the relationship between actuation force F and strain ϵ (see the Supporting Information for a detailed derivation)

$$F = \frac{\epsilon V^2 W}{t} \frac{v}{WL^2} \frac{\alpha^3 \cos(\alpha)}{(\alpha - \sin(\alpha) \cos(\alpha))^2} \quad (1)$$

$$\epsilon = 1 - \frac{\alpha_0}{\alpha} \frac{\sin(\alpha)}{\sin(\alpha_0)} \quad (2)$$

In Equation (1), ϵ and t are the dielectric permittivity and thickness of the shell material, V the applied voltage, L and W the length and width of the shell, and v the volume of dielectric liquid. The variable α in Equations (1) and (2) parameterizes the shape of the shell and ranges between $\alpha = \alpha_0$ (when the actuator is completely unzipped) and $\alpha = \pi/2$ (the maximum stroke). The value of α_0 can be calculated from $v = L^2 W [\alpha_0 - 0.5 \sin(2\alpha_0)] / (2\alpha_0^2)$.

Figure 2d compares the experimental and the calculated load–strain curves. All calculated curves follow the experimental curves, but the experimentally measured strains are, on average, 40% smaller than the strains predicted by the model. We attribute the differences between the theoretical strain and the experimental strain to the side constraints of the actuator and the constraints at the transition zone between the zipping and contracting regions. During actuation, the cross section of the zipping regions flattens, while the cross section of the contracting region takes a more circular shape; this mismatch in shape change leads to buckling of the shell and ultimately constrains the contracting region, which further leads to a loss in the experimentally achieved actuation strain. The model neglects the transition zone between the zipping region and the contracting region, and thus overestimates the actuation strain.

The model indicates how the force output of the actuator can be improved. The first factor on the right-hand side of Equation (1) ($\epsilon V^2 W/t$) is a measure for the electrostatic force inside the zipped region of the electrodes. The second factor $v/(WL^2)$ is the ratio between the volume of the liquid dielectric and the dimensions of the rectangular shell. Keeping $v/(WL^2)$ constant, the strength of the actuator may be increased by increasing the applied voltage, making the actuator wider, or using shell materials with higher permittivity or lower thickness. Decreasing the fill volume also increases the strength of the actuator (Figure S2, Supporting Information) as it not only influences Equation (1) but also leads to a decrease of α_0 .

2.2.3. Dynamic Characteristics

We also characterized the dynamic characteristics of a single unit HS-Peano-HASEL actuator. Figure S3 (Supporting Information) plots the peak strain rate as a function of the load, with a maximum value of 2176% s^{−1} at a load of 0.2 N. The

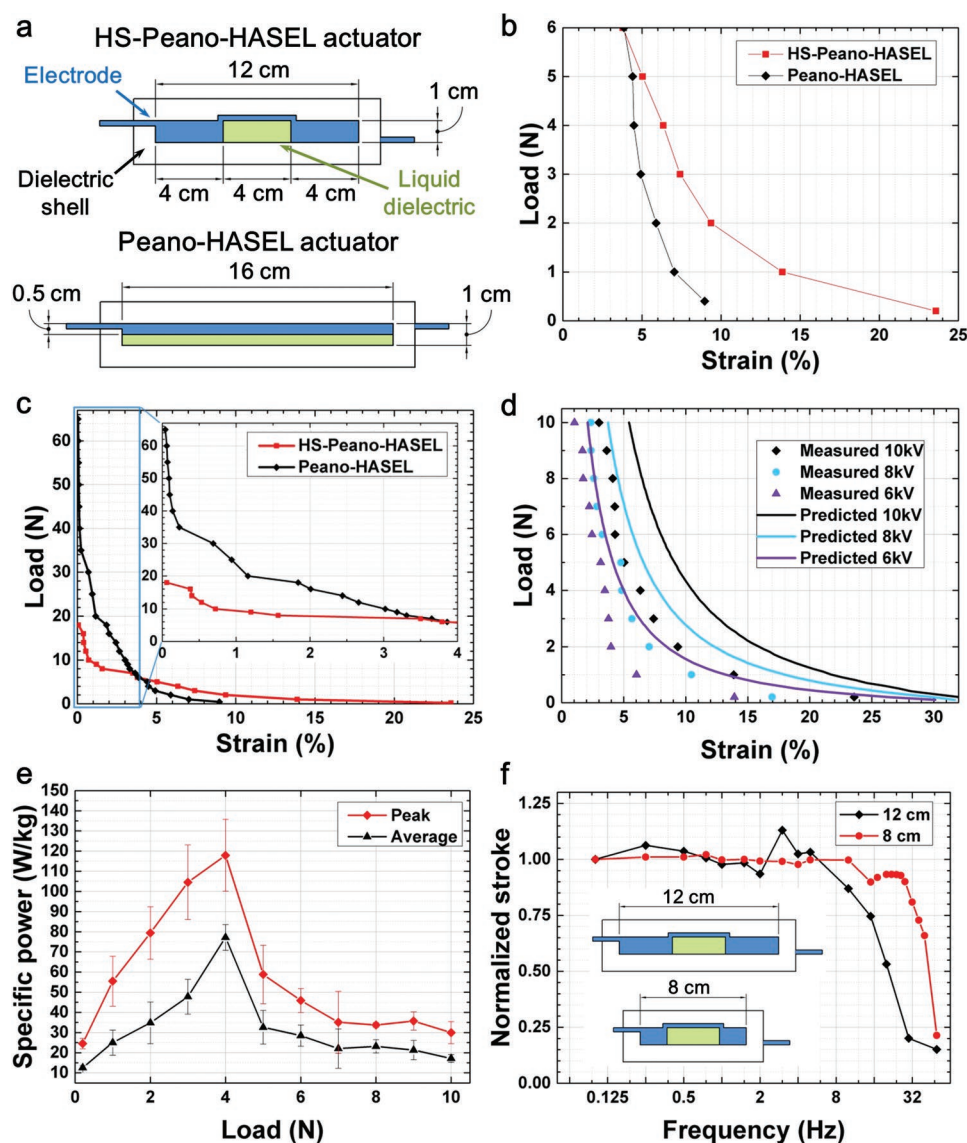


Figure 2. Static and dynamic performance of HS-Peano-HASEL actuators. a) Schematic of HS-Peano-HASEL actuators and Peano-HASEL actuators which were used for experiments. Both types of actuators are designed to have the same mass, length, and maximum capacitance (electrical energy input). b) Comparison of the load–strain characteristics between an HS-Peano-HASEL actuator and a Peano HASEL actuator when operated at 10 kV. For loads up to 6 N, the strain of the HS-Peano-HASEL actuator exceeded the strain of the Peano-HASEL actuator. The maximum strain of the HS-Peano-HASEL was $\approx 24\%$. c) Comparison of the load–strain curves of the HS-Peano-HASEL and the Peano-HASEL over the full range of loads up to the blocking force. The inset figure shows that the Peano-HASEL actuator could lift higher loads at strains up to $\approx 4\%$. d) Comparison of the measured and predicted load–strain characteristics of an HS-Peano-HASEL actuator. e) Peak and average specific power of an HS-Peano-HASEL as a function of load when driven by a 10 kV square-wave voltage signal. f) Frequency response of the HS-Peano-HASEL actuator changed with the width of the actuator. Both actuators had the same width and length of the contracting region and the same volume of liquid dielectric.

peak specific power of the actuator was 117.90 W kg^{-1} and the average specific power reached 77.15 W kg^{-1} at a load of 4 N (Figure 2e; Figure S4, Supporting Information).

We obtained the frequency response of HS-Peano-HASEL actuators using a rubber band to avoid the influence of inertia from hanging weights.^[32] An acrylic mount with a hook with adjustable height was used to mount the actuator to the rubber band (Figure S5, Supporting Information), which acted as an elastic restoring force. The band was prestretched and calibrated with a force gauge to apply an average force of 1 N in the direction of contraction. The actuation stroke under this load was

plotted against the actuation frequency (Figure 2f) and normalized to the stroke at 0.125 Hz (1.39 mm stroke, 13.87% strain). A single unit HS-Peano-HASEL with a width of 12 cm demonstrated a roll-off frequency of 20 Hz. We also compared the frequency response of an 8 cm wide actuator to the 12 cm wide actuator while keeping the dimension of the contracting region and the amount of liquid dielectric within the shell identical (inset image in Figure 2f). The 8 cm wide actuator demonstrated a larger bandwidth with a roll-off frequency over 40 Hz. These results indicate that the frequency response of the actuator can be improved by decreasing the distance over which the liquid

dielectric is displaced within the zipping regions. For comparison, we also measured the dynamic performance (Figure S6, Supporting Information) of the Peano-HASEL actuator introduced in Figure 2a. The peak strain rate was $6070\% \text{ s}^{-1}$ under a 0.2 N load (Figure S6a, Supporting Information) while the peak and average specific power reached 364.70 and 178.53 W kg^{-1} under a load of 2 N (Figure S6b, Supporting Information). The values of the Peano-HASEL actuator are larger than for the HS-Peano-HASEL actuator because the liquid dielectric was displaced over a longer distance in the HS-Peano-HASEL actuator, which leads to a slower response. However, the roll-off frequency of the Peano-HASEL actuator was $\approx 15 \text{ Hz}$ (Figure S6c, Supporting Information), similar to the result for the HS-Peano-HASEL actuator; we hypothesize that this experimental observation stems from inhomogeneous zipping of the electrodes occurring in the Peano-HASEL actuator.^[33]

2.3. Multiunit HS-Peano-HASEL Actuators

2.3.1. Thermoplastic Polyurethane as Dielectric Shell Material

The overall stroke of an actuator can be adjusted by varying the number of actuation units in series; **Figure 3a** shows a four-unit HS-Peano-HASEL actuator, which uses biaxially oriented polypropylene (BOPP) as the shell material and rectangular electrodes made from hydrogel sheets.^[34] The mechanical constraints between the zipping regions and the contracting regions caused a decline of actuation strain of multiunit

HS-Peano-HASEL actuators compared to single-unit actuators (blue curve in Figure 3c). The actuator in the “Voltage on” state in Figure 3a exhibited out-of-plane deformation in the interfacial region between the zipping regions and the contracting regions, indicating that the actuator needed to work against the bending stiffness of the shell material, thereby experiencing a decrease in the maximum strain.

To reduce the impact of out-of-plane deformation on actuation strain, we replaced the BOPP used to fabricate the dielectric shell with a more compliant thermoplastic polyurethane (TPU) (Figure 3b). The TPU film was about twice as thick as BOPP but at the same time, the relative permittivity of TPU was about three times that of BOPP, so that we expected very similar load–strain characteristics based on the model. A four-unit actuator made from TPU reached a strain of 16.03% at 10 kV under a load of 0.2 N (red curve in Figure 3c), compared to a BOPP-based actuator which achieved only 9.36% strain under the same conditions. However, we observed that the HS-Peano-HASEL actuators made from TPU lifted lower loads compared to the BOPP-based actuators in the low-strain region (Figure 3d). We attributed this observation to trapping of liquid dielectric in discrete regions of the shell which were separated by buckling traces (Figure S7, Supporting Information), and prevented the electrodes from zipping uniformly. To ensure consistent experimental conditions for actuators based on BOPP and TPU, we utilized hydrogel electrodes in Figure 3. The solvent required for application of the carbon inks used for all other experiments in this paper adversely affected the mechanical and dielectric properties of TPU.

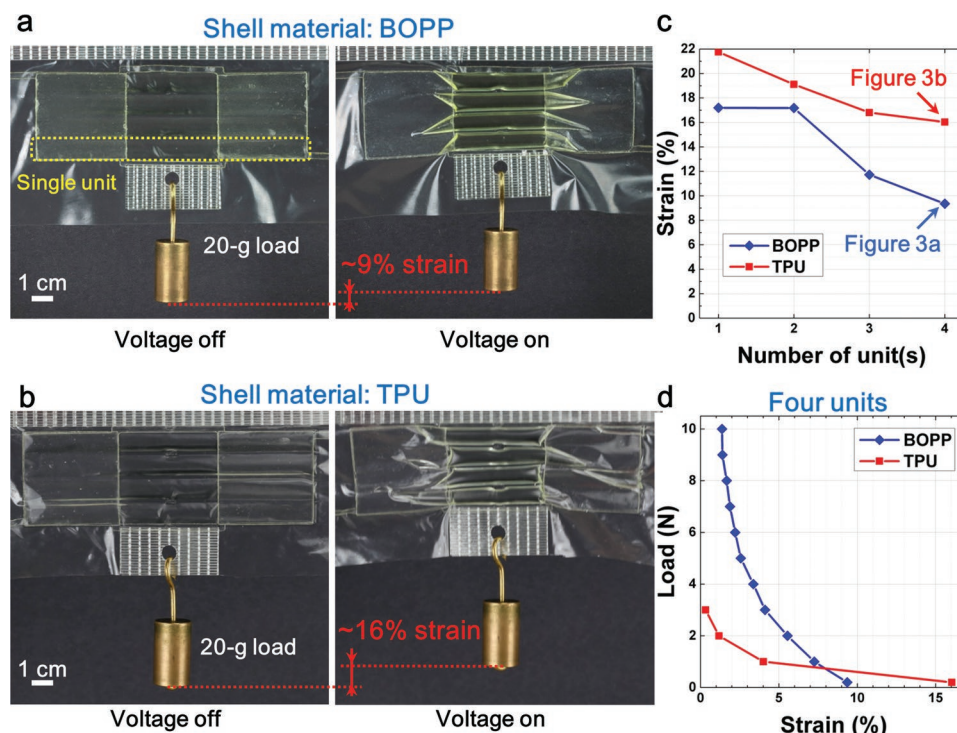


Figure 3. Exploration of different shell materials of multiunit HS-Peano-HASEL actuators. a) A four-unit HS-Peano-HASEL actuator built with BOPP as the shell material contracted by $\approx 9\%$ at 10 kV . b) The actuation strain of a four-unit actuator with TPU as the shell material was $\approx 16\%$ at 10 kV . c) Comparison of the actuation strain of actuators made from BOPP and TPU as a function of the numbers of units under a 20 g load at 10 kV . d) Comparison of the load–strain curves of four-unit HS-Peano-HASELs made from BOPP and TPU operated at 10 kV .

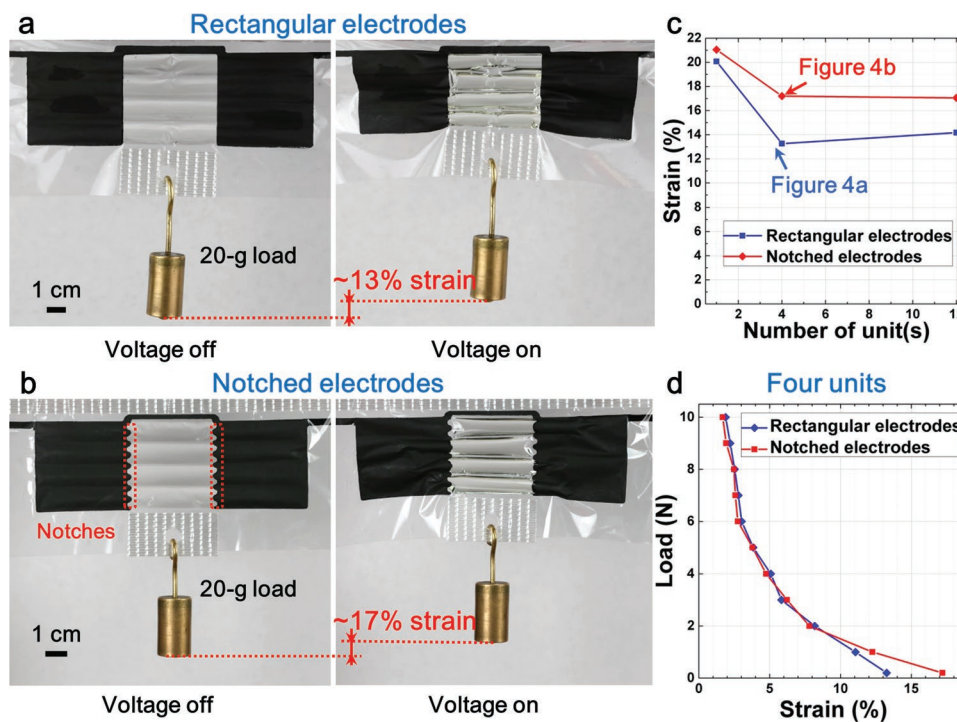


Figure 4. Influence of the shape of the electrode geometries on the load–strain characteristics of multiunit HS-Peano-HASEL actuators. a) A four-unit HS-Peano-HASEL actuator using rectangular screen-printed electrodes reached a strain of $\approx 13\%$ at 10 kV. b) A four-unit actuator using notched screen-printed electrodes contracted by $\approx 17\%$ at 10 kV. c) Comparison of the actuation strains of rectangular and notched screen-printed electrodes as a function of the number of units under a 20 g load at 10 kV. d) Comparison of the load–strain curves of four-unit HS-Peano-HASELs with rectangular and notched screen-printed electrodes at 10 kV.

2.3.2. Notched Electrodes

Another approach to reduce the impact of out-of-plane deformation on actuation strain is to alter the geometry of the electrodes. We developed a notched geometry for the electrodes that leads to controlled buckling to reduce the mechanical constraints between the zipping regions and the contracting regions at low loads. Compared to the rectangular screen-printed electrodes (Figure 4a), notched screen-printed electrodes (Figure 4b) reduced the decline of the actuation strain when increasing the number of actuation units for a BOPP-based actuator (Figure 4c). A four-unit HS-Peano-HASEL actuator under a 20 g load and operated at 10 kV achieved 17.20% strain with notched electrodes and 13.26% strain with rectangular electrodes. When the actuator was scaled to 12 units, it maintained a strain of 17.05% with notched electrodes (Figure 4c; Movie S1, Supporting Information). The load–strain curves of four-unit actuators based on rectangular and notched electrodes show that notched electrodes are advantageous compared to rectangular electrodes in the low-load region (Figure 4d). The screen-printed carbon electrodes are easier to fabricate^[28] and help the actuators achieve larger strains because they reduce the bending stiffness of the shell–electrode bilayer compared to hydrogel electrodes with inextensible BOPP backing. Thus, the screen-printed electrodes facilitate buckling in the transition zones between the zipping and contracting regions. Consequently, the actuator with rectangular electrodes made from carbon paint achieved $\approx 13\%$ strain (Figure 3a) while it only achieved $\approx 9\%$ strain

when hydrogel electrodes were used (Figure 4a). However, we also tested notched hydrogel electrodes (Figure S8, Supporting Information). These results show that the notched geometry of electrodes improves the strain of multiunit HS-Peano-HASEL actuators regardless of the material of electrodes. The notched electrodes had the same area as the rectangular electrodes.

2.4. Artificial Circular Muscle (ACM)

Circular muscles play an important role in biological systems. They enable the primordial heart in ascidians^[35] to pump; they generate peristalsis in earthworms^[36] and digestive tracts,^[37] and regulate flow as sphincters.^[38] We demonstrated an ACM using a 12 unit HS-Peano-HASEL actuator that was rolled around a silicone rubber tube. Figure 5a shows the idealized actuation mechanism, where the length change of the actuator corresponds to a change of the cross-sectional area. At the maximum actuation strain, the area theoretically decreases to $\approx 41\%$ of the initial area. When considering the radial expansion of each of the individual shells, the area of the inscribed circle decreases further. Figure 5b and Movie S2 (Supporting Information) show the actuation behavior of the device. To force the ACM to return to its initial state after an actuation cycle, the silicone rubber tube was prepressurized through a check valve with air (Figure S9, Supporting Information). In contrast to most engineered systems, which perform continuous pumping,^[39] the ACM system performed biomimetic pulsed pumping, resembling the motion

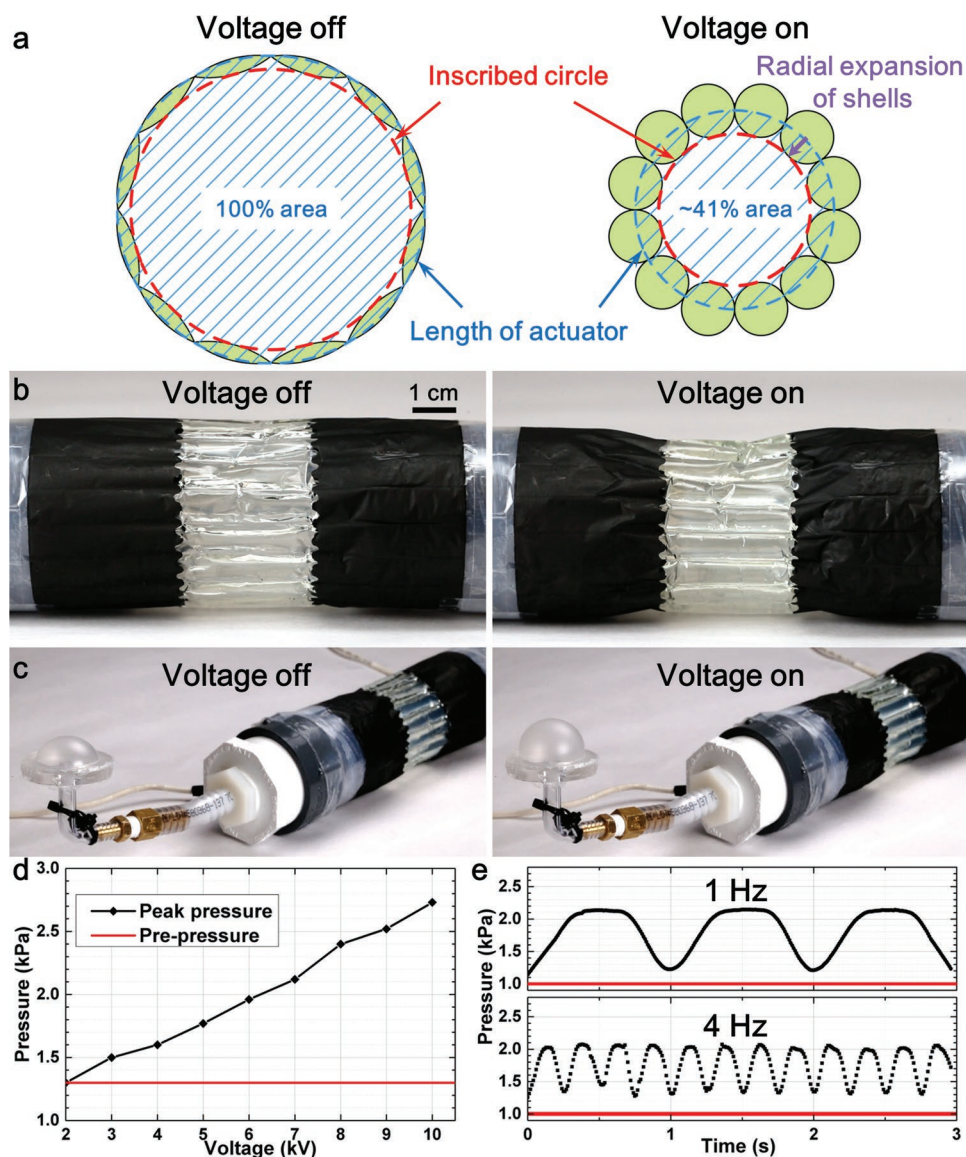


Figure 5. An artificial circular muscle (ACM) constructed using a 12 unit HS-Peano-HASEL actuator. a) An idealized schematic of the ACM shows that the circular area enclosed by the actuator theoretically decreases to $\approx 41\%$ of its initial area when actuated. b) Deformation of the ACM at 10 kV. c) Actuated at 10 kV, the ACM pumped air into an elastic diaphragm. d) Increase of the pressure within the system as a function of voltage applied to the ACM. e) Pressure–time curves of the system at 1 and 4 Hz.

of the primordial heart of ascidians;^[35] we demonstrated the pumping behavior by inflating a thin elastic diaphragm made from silicone (Figure 5c; Movie S2, Supporting Information). We measured the pressure increase within the chamber when different voltages were applied to the ACM (Figure 5d; Figure S10a, Supporting Information). The chamber was initially pressurized to 1.30 kPa (ΔP_0 in Figure S8b, Supporting Information) to provide a restoring force and adequate contact between the internal silicone tube and the ACM. The pressure within the chamber increased proportionally to the applied voltage and reached a maximum of 2.73 kPa at 10 kV (Figure S10b, Supporting Information). Additionally, the ACM was driven by a sinusoidal waveform at various frequencies with an initial pressure of 1.00 kPa (Figure 5e). The ACM generated a blocking pressure differential

of 0.94 kPa at 1 Hz and 0.84 kPa at 4 Hz. We measured the flow rate of the ACM (Figure S11a, Supporting Information). Driven by a 4 Hz sinusoidal voltage signal with a 10 kV amplitude, the peak and average flow rates during contraction of the ACM were 2.30 L min⁻¹ (Figure S11b, Supporting Information) and 1.47 L min⁻¹ (Figure S11c, Supporting Information), respectively. For these flow rates, the system pressure oscillated between 1.5 and 1.8 kPa above atmosphere.

2.5. Strain-Amplifying Pulley System

In most applications, artificial muscles must anchor to a rigid structure to effectively exert a force. Here, we introduce

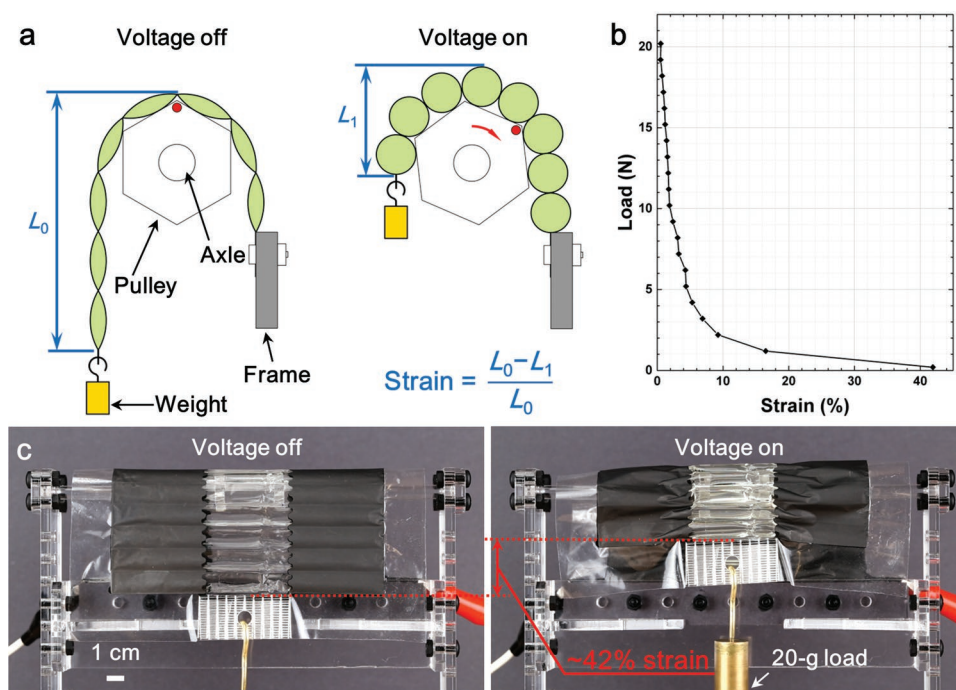


Figure 6. A strain-amplifying pulley system. a) Schematic of the pulley system. b) Load–strain curve of a 12 unit HS-Peano-HASEL actuator using the pulley system with the actuator operated at 10 kV. c) At 10 kV, the pulley system amplified the actuation strain from $\approx 17\%$ (Figure 1c) to $\approx 42\%$ with a 20 g load.

a strain-amplifying pulley system that more than doubles the actuation strain of an HS-Peano-HASEL actuator (Figure S12, Supporting Information). A multiunit HS-Peano-HASEL actuator was fixed on the frame and was hung over an acrylic pulley (Figure 6a). We used a regular hexagon as the wheel of the pulley so that a corner of the hexagon pulley nested between two units of the actuator. This system allows the actuator to maintain its stroke, while decreasing the effective length of the actuator (L_0). Figure 6b shows the load–strain curve of a 12 unit HS-Peano-HASEL actuator using the pulley system with the actuator operated at 10 kV. The actuator achieved 42% strain (as opposed to 17% strain without the pulley system) under a 20 g load and a blocking force larger than 20 N. Figure 6c and Movie S3 (Supporting Information) demonstrate the actuation of a 12 unit actuator mounted to a strain-amplifying pulley system that achieved actuation strain matches the maximum strain of natural muscle.^[31]

3. Conclusion

We introduced an electrohydraulically driven, linearly contractile soft actuator which achieved linear strain exceeding 20% (the typical value for skeletal muscle). Specifically, the HS-Peano-HASEL actuator introduced in this paper achieved maximum linear strains of $\approx 24\%$, exceeding the maximum strain of $\approx 15\%$ of Peano-HASEL actuators.^[29,30] Material and design variations were utilized to improve the stroke of multiunit HS-Peano-HASEL actuators. The demonstration of the ACM highlights potential applications in artificial organs^[40] and soft pumps. A strain-amplifying pulley system can be used for

applications requiring large deformations in a compact space such as animatronic faces.^[41]

The experimental results for the load–strain behavior follow the trend predicted by the analytical model we developed. The deviation between experimental results and theoretical predictions is attributed to the constraints at the intersection of the contracting region and the zipping regions, which are neglected in the model and lead to an overestimation of strain.

The actuation mechanism of HS-Peano-HASELS necessitates actuation units with relatively large widths which will be a drawback for certain applications. On the other hand, when compared to multiunit Peano-HASELS, multiunit HS-Peano-HASELS do not have gaps between electrodes of single units, which simplifies the manufacturing process of the electrodes of multiunit HS-Peano-HASEL actuators.

Overall, the ability to achieve muscle-like linear contraction and all-around performance highlights the potential of HS-Peano-HASEL actuators for wide use in future bioinspired robotic systems.

Supporting Information

Supporting Information is available from the Wiley Online Library or from the author.

Acknowledgements

The authors would like to thank N. Kellaris and E. Acome for advice with performance testing of actuators. The authors would also like to thank S. Humbert for the use of high-speed camera equipment (Phantom

v710 and high-power tungsten flood lights). X.W. acknowledges financial support from the Joint Doctoral Training Program (No. 201706260025) of the China Scholarship Council. S.K.M. was supported through the NASA Innovative Advanced Concepts program (No. 80NSSC18K0962). C.K., P.R., and E.H.R. acknowledge support from a Packard Fellowship from The David and Lucile Packard Foundation, from the NSF EFRI Research Projects (Grant No. 1830924), and from the University of Colorado Boulder. The authors also acknowledge funding from the Army Research Office (Grant No. W911NF-18-1-0203), which was used to purchase laboratory equipment to characterize and fabricate actuators.

Conflict of Interest

S.K.M. and C.K. are co-founders of Artimus Robotics, a start-up company commercializing HASEL actuators. C.K., X.W., and S.K.M. are listed as the inventors of a provisional patent covering the ideas presented in this paper.

Keywords

artificial muscles, bioinspired designs, HASEL actuators, soft pump, soft robotics

Received: October 24, 2019

Revised: November 21, 2019

Published online: December 15, 2019

- [1] G.-Z. Yang, J. Bellingham, P. E. Dupont, P. Fischer, L. Floridi, R. Full, N. Jacobstein, V. Kumar, M. McNutt, R. Merrifield, B. J. Nelson, B. Scassellati, M. Taddeo, R. Taylor, M. Veloso, Z. L. Wang, R. Wood, *Sci. Rob.* **2018**, 3, eaar7650.
- [2] P. Polygerinos, N. Correll, S. A. Morin, B. Mosadegh, C. D. Onal, K. Petersen, M. Cianchetti, M. T. Tolley, R. F. Shepherd, *Adv. Eng. Mater.* **2017**, 19, 1700016.
- [3] D. Trivedi, C. D. Rahn, W. M. Kier, I. D. Walker, *Appl. Bionics Biomech.* **2008**, 5, 99.
- [4] C. Lee, M. Kim, Y. J. Kim, N. Hong, S. Ryu, H. J. Kim, S. Kim, *Int. J. Control Autom. Syst.* **2017**, 15, 3.
- [5] C. Laschi, B. Mazzolai, M. Cianchetti, *Sci. Rob.* **2016**, 1, eaah3690.
- [6] P. Polygerinos, Z. Wang, K. C. Galloway, R. J. Wood, C. J. Walsh, *Rob. Auton. Syst.* **2015**, 73, 135.
- [7] R. Pelrine, R. Kornbluh, Q. Pei, J. Joseph, *Science* **2000**, 287, 836.
- [8] A. O'Halloran, F. O'Malley, P. McHugh, *J. Appl. Phys.* **2008**, 104, 071101.
- [9] R. Pelrine, Q. Pei, R. D. Kornbluh, *Proc. SPIE* **2018**, 10594, 1059406.
- [10] G.-Y. Gu, J. Zhu, L.-M. Zhu, X. Zhu, *Bioinspir. Biomim.* **2017**, 12, 011003.
- [11] I. A. Anderson, T. A. Gisby, T. G. McKay, B. M. O'Brien, E. P. Calius, *J. Appl. Phys.* **2012**, 112, 041101.
- [12] F. Daerden, D. Lefeber, *Eur. J. Mech. Environ. Eng.* **2002**, 47, 11.
- [13] R. F. Shepherd, F. Ilievski, W. Choi, S. A. Morin, A. A. Stokes, A. D. Mazzeo, X. Chen, M. Wang, G. M. Whitesides, *Proc. Natl. Acad. Sci. USA* **2011**, 108, 20400.
- [14] R. V. Martinez, C. R. Fish, X. Chen, G. M. Whitesides, *Adv. Funct. Mater.* **2012**, 22, 1376.
- [15] D. Yang, M. S. Verma, J.-H. So, B. Mosadegh, C. Keplinger, B. Lee, F. Khashai, E. Lossner, Z. Suo, G. M. Whitesides, *Adv. Mater. Technol.* **2016**, 1, 1600055.
- [16] C. Keplinger, T. Li, R. Baumgartner, Z. Suo, S. Bauer, *Soft Matter* **2012**, 8, 285.
- [17] Y. Chen, H. Zhao, J. Mao, P. Chirarattananon, E. F. Helbling, N.-P. Hyun, D. R. Clarke, R. J. Wood, *Nature* **2019**, 575, 324.
- [18] C. Keplinger, M. Kaltenbrunner, N. Arnold, S. Bauer, *Appl. Phys. Lett.* **2008**, 92, 192903.
- [19] S. Diahm, S. Zelmat, M.-L. Locatelli, S. Dinculescu, M. Decup, T. Lebey, *IEEE Trans. Dielectr. Electr. Insul.* **2010**, 17, 18.
- [20] S. Li, D. M. Vogt, D. Rusc, R. J. Wood, *Proc. Natl. Acad. Sci. USA* **2017**, 114, 13132.
- [21] S. Sanan, P. S. Lynn, S. T. Griffith, *J. Mech. Robot.* **2014**, 6, 031003.
- [22] F. Ilievski, A. D. Mazzeo, R. F. Shepherd, X. Chen, G. M. Whitesides, *Angew. Chem.* **2011**, 123, 1930.
- [23] M. A. Robertson, J. Paik, *Sci. Rob.* **2017**, 2, eaan6357.
- [24] Z. Jiao, C. Ji, J. Zou, H. Yang, M. Pan, *Adv. Mater. Technol.* **2019**, 4, 1800429.
- [25] G. M. Whitesides, *Angew. Chem., Int. Ed.* **2018**, 57, 4258.
- [26] M. T. Tolley, R. F. Shepherd, B. Mosadegh, K. C. Galloway, M. Wehner, M. Karpelson, R. J. Wood, G. M. Whitesides, *Soft Rob.* **2014**, 1, 213.
- [27] E. Acome, S. K. Mitchell, T. G. Morrissey, M. B. Emmett, C. Benjamin, M. King, M. Radakovitz, C. Keplinger, *Science* **2018**, 359, 61.
- [28] S. K. Mitchell, X. Wang, E. Acome, T. Martin, K. Ly, N. Kellaris, V. G. Venkata, C. Keplinger, *Adv. Sci.* **2019**, 6, 1900178.
- [29] N. Kellaris, V. G. Venkata, P. Rothmund, C. Keplinger, *Extreme Mech. Lett.* **2019**, 29, 100449.
- [30] N. Kellaris, V. G. Venkata, G. M. Smith, S. K. Mitchell, C. Keplinger, *Sci. Rob.* **2018**, 3, eaar3276.
- [31] J. D. W. Madden, N. A. Vandesteeg, P. A. Anquetil, P. G. A. Madden, A. Takshi, R. Z. Pytel, S. R. Lafontaine, P. A. Wieringa, I. W. Hunter, *IEEE J. Oceanic Eng.* **2004**, 29, 706.
- [32] F. Carpi, I. Anderson, S. Bauer, G. Frediani, G. Gallone, M. Gei, C. Graaf, C. Jean-Mistral, W. Kaal, G. Kofod, M. Kolloosche, R. Kornbluh, B. Lassen, M. Matysek, S. Michel, S. Nowak, B. O'Brien, Q. Pei, R. Pelrine, B. Rechenbach, S. Rosset, H. Shea, *Smart Mater. Struct.* **2015**, 24, 105025.
- [33] P. Rothmund, N. Kellaris, C. Keplinger, *Extreme Mech. Lett.* **2019**, 31, 100542.
- [34] C. Keplinger, J.-Y. Sun, C. C. Foo, P. Rothmund, G. M. Whitesides, Z. Suo, *Science* **2013**, 341, 984.
- [35] R. D. Barnes, *Invertebrate Zoology*, Holt-Saunders International, Philadelphia, PA **1982**.
- [36] C. A. Edwards, P. J. Bohlen, *Biology and Ecology of Earthworm*, Chapman & Hall, London, UK **1996**.
- [37] S. K. Sarna, *Colonic Motility: From Bench Side to Bedside*, Morgan & Claypool Life Sciences, Williston, NT **2010**.
- [38] A. J. Vander, J. H. Sherman, D. S. Luciano, *Human Physiology: The Mechanisms of Body Function*, McGraw-Hill, New York, NY **1998**.
- [39] V. Cacucciolo, J. Shintake, Y. Kuwajima, S. Maeda, D. Floreano, H. Shea, *Nature* **2019**, 572, 516.
- [40] R. H. Baughman, *Science* **2005**, 308, 63.
- [41] Y. Tadesse, S. Priya, H. Stephanou, D. Popa, D. Hanson, *Ferroelectrics* **2006**, 345, 13.